

Two-dimensional hybrid MHD-kinetic electron simulations of an Alfvén wave pulse

P. A. Damiano and A. N. Wright

Mathematical Institute, University of St. Andrews, St. Andrews, UK

Received 31 May 2004; revised 16 September 2004; accepted 21 October 2004; published 7 January 2005.

[1] A two-dimensional hybrid MHD-kinetic model incorporating kinetic electrons is used to simulate a shear Alfvén wave pulse propagating in a constant density plasma and magnetic field. The pulse is rectangular in shape so that the perpendicular and parallel current regions are distinct. Two regimes are considered: the large-scale limit where the perpendicular-scale length $L_{\perp} \gg \lambda_e$ and the “inertial limit” ($L_{\perp} \leq 10\lambda_e$). In addition, a potential-current relation is derived from consideration of electron energy in the wave frame. It is found that the parallel electron current is carried by a uniform acceleration of the entire distribution function where larger current is carried by a correspondingly larger displacement. In the inertial limit the original rectangular shape of the pulse is distorted by a broadening and narrowing in the perpendicular direction at the leading and trailing edges, respectively, of the pulse, as well as by the propagation away from the corners of inertial Alfvén waves with perpendicular wavelengths of the order of $10\lambda_e$ (Alfvén resonance cones). In both limits, and in spite of the added structure in the inertial case, the parallel electric field calculated from a derived “effective” potential reproduces the simulation parallel electric field accurately.

Citation: Damiano, P. A., and A. N. Wright (2005), Two-dimensional hybrid MHD-kinetic electron simulations of an Alfvén wave pulse, *J. Geophys. Res.*, 110, A01201, doi:10.1029/2004JA010603.

1. Introduction

[2] The link between Alfvén waves (either as pulses or standing modes) and auroral arcs has been well established using both ground-based and satellite observations [Xu *et al.*, 1993; Lotko *et al.*, 1998; Chaston *et al.*, 2002; Samson *et al.*, 2003]. Associated with these waves are field-aligned currents of up to several $\mu\text{A}/\text{m}^2$ carried primarily by electron beams with energies in the keV range. These beams are accelerated by field-aligned electric fields of the order of mV/m in the auroral acceleration region ($1-3 R_E$ altitude).

[3] In the traditional MHD limit, $m_e \rightarrow 0$, and there is no parallel electric field to accelerate electrons. However, for straight field lines, with the inclusion of electron mass in the single-fluid picture via the generalized Ohm’s law [Goertz and Boswell, 1979; Wei *et al.*, 1994; Wright *et al.*, 2002], inertial effects become important on the order of the scale length perpendicular to the ambient magnetic field $L_{\perp} \leq 10\lambda_e$ ($k_{\perp}\lambda_e = (2\pi/L_{\perp})\lambda_e \sim 1$), where $\lambda_e = \sqrt{m_e/\mu_0 n e^2}$ is the electron inertial length. The MHD approach alone, however, neglects potentially important effects such as mirror force contributions [Rankin *et al.*, 1999; Rönmark, 2002] and does not provide any information about the structure and evolution of the electron distribution functions [Wright and Hood, 2003]. This has led to approaches that use the Vlasov equation to describe the electron population [Rankin *et al.*,

1999; Wright and Hood, 2003] or more numerical methods using kinetic electrons [Hui and Seyler, 1992; Thompson and Lysak, 1996; Chaston *et al.*, 2000, 2002, 2003; Damiano *et al.*, 2003; P. A. Damiano *et al.*, Hybrid MHD-kinetic electron closure methods and shear Alfvén waves in nonuniform plasmas, submitted to *Physics of Plasmas*, 2004, hereinafter referred to as Damiano *et al.*, submitted manuscript, 2004].

[4] The two-dimensional (2-D) model developed by Damiano *et al.* [2003, also submitted manuscript, 2004] incorporates the full set of cold plasma MHD equations and kinetic electrons using the guiding center equations as the equations of motion. In this paper we will use the model to consider the case of an Alfvén wave pulse propagating in a constant density plasma and magnetic field in both the large perpendicular-scale length limit ($L_{\perp} \gg \lambda_e$) and “inertial regimes” ($L_{\perp} \leq 10\lambda_e$). The parameters chosen will be representative of those in the auroral acceleration region. In addition, a potential-parallel current density relation is derived using conservation of electron energy arguments in the frame of reference of the pulse, and the parallel electric field calculated from the potential is compared directly with that produced from the simulation.

[5] The rest of the paper is broken up into five main sections. Section 2 highlights the hybrid model. Section 3 will present the large perpendicular-scale simulation results along with the derivation of the potential-current relation, while section 4 summarizes the simulation results for the inertial limit. Section 5 compares the energy densities of the

different components, and section 6 has the concluding summary and discussion.

2. Hybrid Model

[6] The 2-D Cartesian hybrid model used is based on the model summarized by *Damiano et al.* [2003] with some modifications as discussed by Damiano et al. (submitted manuscript, 2004). It solves explicitly in the x and z directions with the ambient magnetic field B_o directed along the z axis. The limited consideration of a y dimension is allowed by specifying a value for the wave number in the y direction k_y (although $k_y = 0$ is used here). The model incorporates the full set of the linear cold plasma MHD equations, but for a toroidal shear Alfvén wave mode with $k_y = 0$, only the equations for the shear velocity u_y and perturbed magnetic field b_y , are needed, given by

$$\frac{\partial u_y}{\partial t} = \frac{B_o}{\mu_o \rho_o} \left(\frac{\partial b_y}{\partial z} \right) \quad (1)$$

$$\frac{\partial b_y}{\partial t} = \frac{\partial E_z}{\partial x} - \frac{\partial E_x}{\partial z}, \quad (2)$$

respectively.

[7] For the electrons, gyroradius effects are negligible for magnetospheric scales, and so the guiding center equations

$$\frac{dv_e}{dt} = -\frac{e}{m_e} E_z \quad (3)$$

$$\frac{dr_{gz}}{dt} = v_e \quad (4)$$

are used as the equations of motion for the electrons parallel to the ambient magnetic field where r_{gz} is the parallel component of the guiding center and v_e is the parallel component of the electron guiding center velocity. The closure between the MHD equations and the kinetic electrons is obtained via the parallel electric field given by a modification of the generalized Ohm's law (*Damiano et al.*, submitted manuscript, 2004),

$$\frac{\partial^2 E_z}{\partial x^2} - \frac{1}{\lambda_e^2} E_z = \frac{\partial}{\partial z} \left(\frac{\partial E_x}{\partial x} \right) + \mu_o e \sum_i v_{ei}^2 S(\mathbf{x}, \mathbf{x}_i) - \frac{1}{\epsilon_o} \frac{\partial}{\partial z} \left[\int_0^t dt \left(\frac{\partial j_x}{\partial x} + \frac{\partial j_e}{\partial z} \right) \right], \quad (5)$$

where $E_x = -u_y B_o$ is the perpendicular electric field from the ideal MHD approximation, $\lambda_e^2 = m_e / (\mu_o n e^2)$ is the electron inertial length, $j_e = -e \sum_i v_{ei} S(\mathbf{x}, \mathbf{x}_i)$ is the parallel electron current, and $S(\mathbf{x}, \mathbf{x}_i)$ is the particle shape function [*Birdsall and Langdon*, 1991]. The second term on the right-hand side is related to the second moment of the electron distribution function, and the last term is related to the quasi-neutrality of the plasma. Without this term the expression is the same as used by *Hui and Seyler* [1992] (where quasi-neutrality was directly assumed) and *Damiano et al.* [2003]. Equation (5) arises from this “traditional” version by considering an expansion of the $\partial E_x / \partial x$ term into a quasi-neutral MHD ($\nabla \cdot \mathbf{j} = 0$) component and a “correction” ($\partial E_x / \partial x = (\partial E_x / \partial x)_{\text{MHD}} + (\partial E_x / \partial x)_c$). The

contribution of this correction (resulting when the parallel electron current differs from the divergence-free MHD solution) can be accounted for using

$$\epsilon_o \frac{\partial}{\partial t} \left(\frac{\partial E_x}{\partial x} \right)_c = -\nabla \cdot \mathbf{j}, \quad (6)$$

which is derived from the divergence of Ampere's law (including displacement term) with the assumptions $\partial / \partial z \ll \partial / \partial x$ and $\partial / \partial y = 0$. Using this to substitute in for $(\partial E_x / \partial x)_c$ then yields equation (5). The low-frequency nature of magnetospheric waves means that the displacement term is generally neglected, but its use works here since the oscillations needed to maintain quasi-neutrality are much shorter than the MHD timescales. It is also used by *Lysak and Song* [2001, 2002] in their model of magnetosphere-ionosphere coupling. In addition, equation (6) can also be derived from the equations of continuity for the electrons and ions and Poisson's equations as given by *Damiano et al.* [2003]. However, it was introduced in a slightly different way than noted here and by *Damiano et al.* (submitted manuscript, 2004).

[8] Both the MHD and guiding center equations are solved using a predictor-corrector method [see *Damiano et al.*, 2003, also submitted manuscript, 2004], and the MHD equations are solved on a set rectangular grid, while the electrons are free to move anywhere in the 2-D space. The grid has constant but different spacing in each direction. The electron density, current, and pressure are interpolated to the grid points using biquadratic spline interpolation [*Birdsall and Langdon*, 1991] represented above by the particle shape function $S(\mathbf{x}, \mathbf{x}_i)$, where \mathbf{x}_i is the position of the i th electron and \mathbf{x} is the grid cell position. The field values are interpolated to the particle positions using the same method.

[9] The magnetic field was normalized by the ambient magnetic field B_o , length was normalized by an Earth radius $L_N = R_E$, density was normalized by the ambient plasma density $\rho_N = n m_p$ (where n is the plasma number density), and velocity was normalized by the ambient Alfvén speed $V_N = B_o / \sqrt{\mu_o \rho_N}$. Using these definitions, time, electric field, and current density were normalized as $t_N = L_N / V_A$, $E_N = V_N B_o$, and $j_N = B_o / (\mu_o L_N)$, respectively. For the simulations presented here the parameters were chosen to be roughly consistent with the auroral acceleration region at an altitude of 1–3 R_E with a constant ambient magnetic field of $B_o = 5000$ nT and a constant number density of $n = 1 \text{ cm}^{-3}$. The simulation electrons were loaded with constant (but different) spacing in the x and z directions. Each electron is a “superparticle” representative of many electrons. The scaling is determined by the ratio of the ambient plasma density and the simulation electron number density [*Damiano et al.*, 2003]. The velocities were assigned to the electrons using a 1-D Maxwellian as a probability distribution function

$$f(v_e) \propto e^{-m_e v_e^2 / 2kT}, \quad (7)$$

where $kT = 100$ eV was used. For these parameters the Alfvén speed is $\sim 10^5$ km/s, and the electron thermal speed ($v_{th} = \sqrt{2kT / m_e}$) is ~ 6000 km/s, and so we are in the cold plasma limit ($V_A \gg v_{th}$).

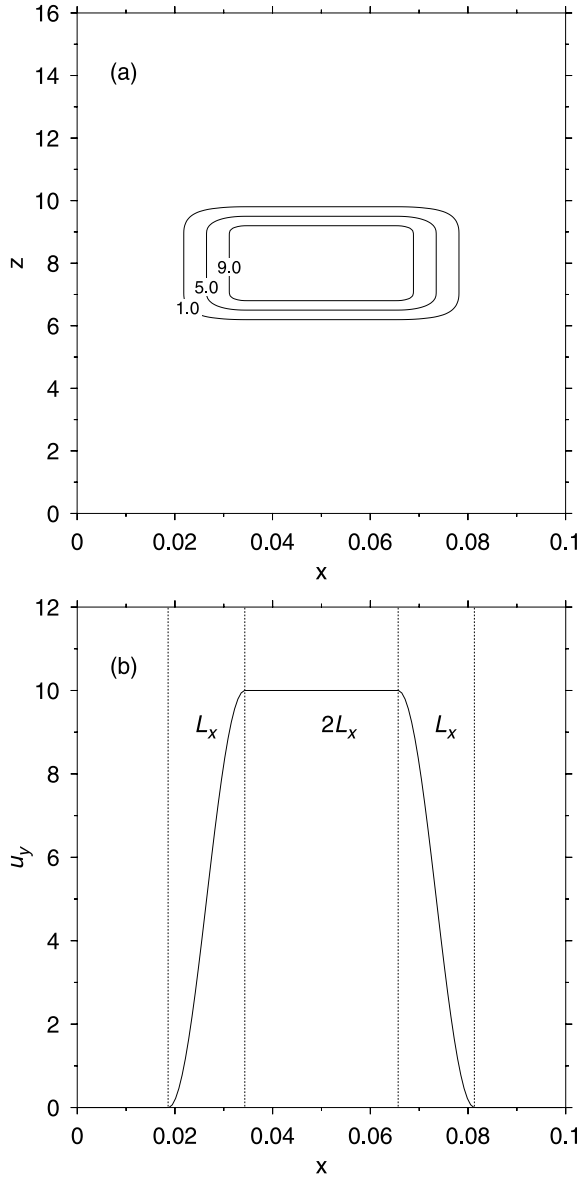


Figure 1. (a) Contours of the initial shear velocity perturbation u_y at $t = 0$ for $L_x = 100$ km. (b) Slice in x along the center of the velocity perturbation.

[10] The system was perturbed by introducing a pulse perturbation in u_y in the center of the simulation grid. To be consistent with values commonly seen in ULF wave phenomena, an initial value of u_y consistent with a perturbed magnetic field value of $b_y = 100$ nT was chosen using the standard Alfvén-Walén [Alfvén, 1942; Walén, 1944; Cross, 1988] relation

$$u_y = \frac{V_A b_y}{B_0}. \quad (8)$$

Figure 1a illustrates a contour plot of the initial pulse perturbation for u_y , while Figure 1b illustrates the envelope found from a slice in the x direction, where L_x is the width of

the region of variation at either edge of the pulse. This edge region was done using a half-period cosine function. A slice in the z direction would illustrate an identical geometry but with the parameter L_z . The general (x, z) variation is found by taking the product of the normalized envelopes in x and z multiplied by the amplitude value of u_y , determined from the Walén relation (8). This idealized shape was chosen to create a current loop around the outside of the pulse region and to clearly distinguish the perpendicular current regions carried by ions from the parallel current regions carried by electrons.

[11] The values of L_x were chosen to represent two distinct limits: the large perpendicular-scale length limit ($L_x \gg \lambda_e$) where electron mass effects are negligible and the “inertial limit” where they are important ($L_x \leq 10\lambda_e$). For the number density $n = 1.0 \text{ cm}^{-3}$, $\lambda_e = 5.3$ km, and so the two cases $L_x = 100$ km ($L_x = 18.86\lambda_e$) and $L_x = 25$ km ($L_x = 4.72\lambda_e$) were chosen. In both cases the value of L_z was chosen to be an Earth radius to roughly correspond to the parallel scale in the auroral acceleration region (although this choice is not of critical importance). Figure 1 illustrates the initial perturbation for $L_x = 100$ km. In the z direction the grid extends from $z = 0$ to 16 in nondimensional units, and 200 grid points are used. The large range is chosen to give the pulse sufficient distance to propagate before reaching the edges (although periodic boundary conditions are used in this direction). In the x direction the grid range is from $x = 0$ to 0.1 for $L_x = 100$ km and from 0 to 0.04 for $L_x = 25$ km. In both cases, 150 grid points were used, and the boundary conditions were open ($\partial/\partial x = 0$), although this was not of importance because the waves do not reach the boundaries during the simulation. For both limits the time step was 2.5×10^{-5} , and the number of simulation electrons used was 15×10^6 (1000 equally spaced initial particle positions in the x direction and 15,000 in z [see Damiano et al., 2003]). With these parameters the percentage change in energy over the length of the run (see section 5) was $5 \times 10^{-2}\%$, illustrating that energy was well conserved. A convergence test was also made by doing a second run for the $L_x = 25$ km case with twice the number of grid points, half the time step, and 24×10^6 simulation electrons. The velocity field u_y was compared with the values from the original run at the end of the simulation ($t = 0.009$, see section 4) using the quantity

$$\frac{\sum_i |u'_{y_i} - u_{y_i}|}{\sum_i |u'_{y_i} + u_{y_i}|/2} \quad (9)$$

to give an estimate of the change in u_y between the two runs. The primed values are from the simulation with increased resolution, and the summation is over the common grid points in the two runs. The error in the fields by this measure was 5%, indicating good convergence.

3. Simulation in the Large-Scale Limit ($L_x = 100$ km)

3.1. Wave Fields, Current, and Distribution Function Evolution

[12] The pulse perturbation introduced at $t = 0$ splits up into two identical pulses propagating away from each other toward the upper and lower z boundaries with speeds V_A and $-V_A$, respectively. For the simulations presented in this

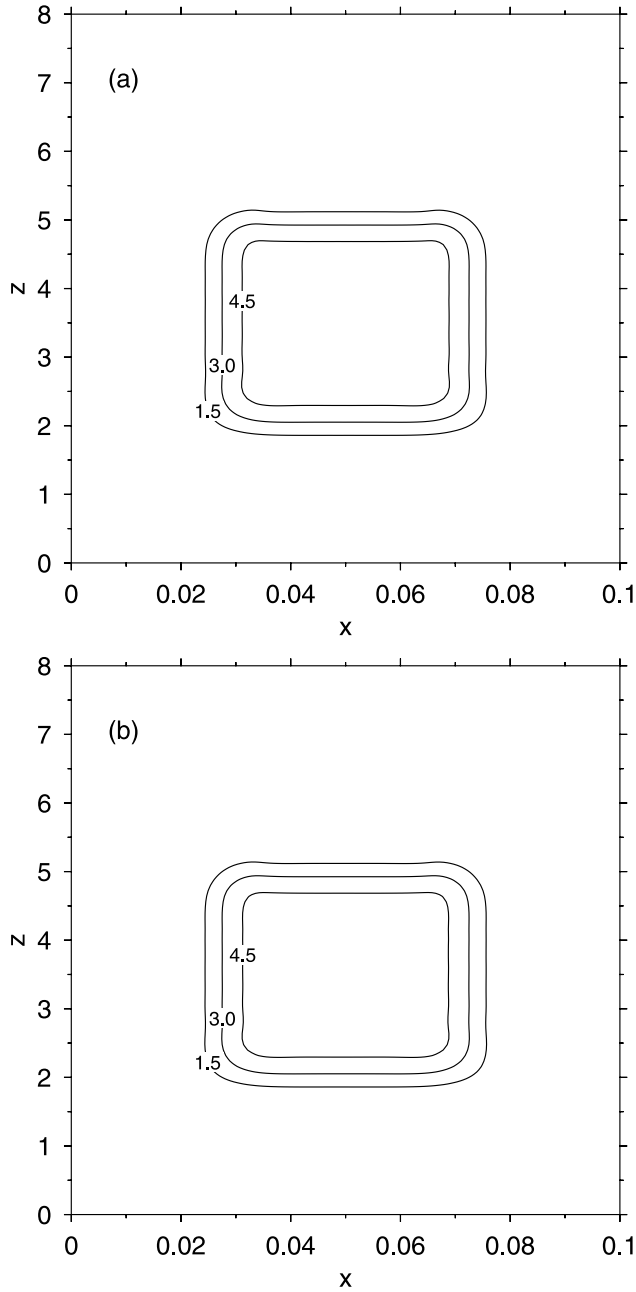


Figure 2. Contours of (a) u_y and (b) b_y at $t = 0.009$ for the $L_x = 100$ km simulation.

section we concentrate on the pulse propagating toward the lower end of the grid, specifically for a snapshot at $t = 0.009$. Figure 2 illustrates contours of u_y and b_y . Both have similar magnitudes, which is to be expected from the Walén relation, and they propagate maintaining the same shape as the initial perturbation with only some minor modifications at the corners. The fact that two identical pulses have split away from the initial pulse is evident in that the magnitude in this case is half of the initial value.

[13] Figure 3 illustrates contour plots of the perpendicular current j_x and parallel current j_e . As expected, they form a current ring around the pulse with perpendicular currents along the top and bottom edges ($j_x = -\partial b_y / \partial z$) closed by

parallel electron current along the left and right edges ($j_e = j_z = \partial b_y / \partial x$). Figure 4 illustrates a slice along the middle of the right-hand negative current region at $x = 0.072$ in combination with a series of plots of the distribution function. The plot is the instantaneous slice at $t = 0.009$. However, it can also be pictured as a series of time slices for an observer sitting at $z = 1$ where the ambient background distribution function is accelerated just as the leading edge of the pulse begins to pass (Figure 4, plot for $z = 2$). This acceleration is manifested by a slight displacement of the entire distribution function to the right. This is consistent with the negative current, as is evident from the definition $j_e = -n_e e \langle v_e \rangle$. As the constant current region passes, the distribution function maintains a constant displacement

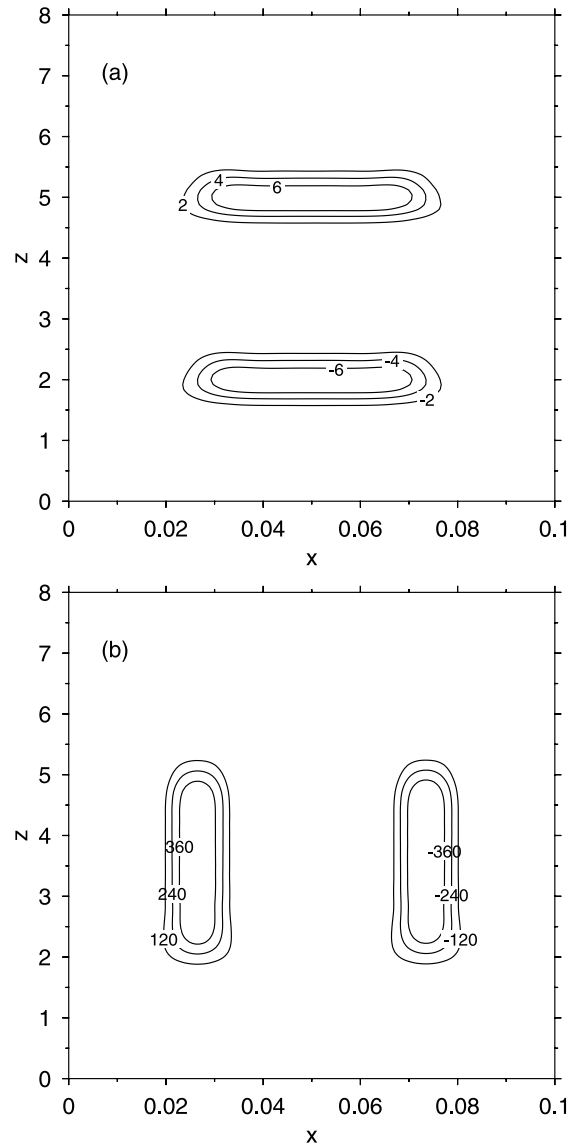


Figure 3. Contours of (a) perpendicular current density j_x and (b) parallel current density j_e at $t = 0.009$ for the $L_x = 100$ km simulation.

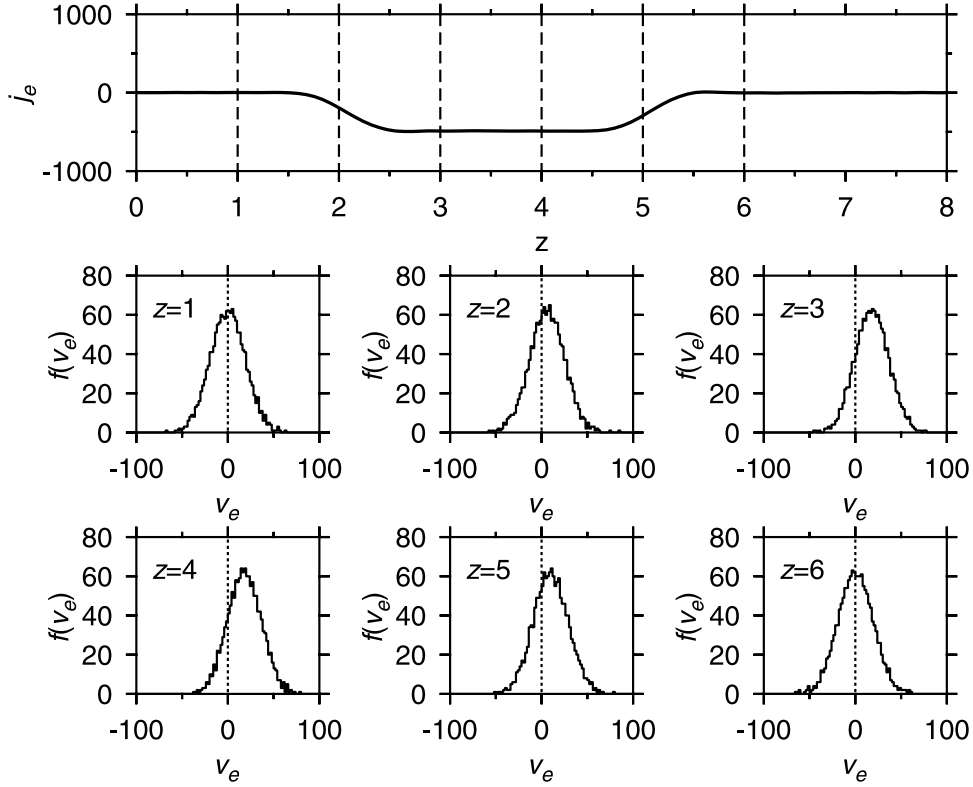


Figure 4. (top) Slice of parallel current density as a function of z at $x = 0.725$ and $t = 0.009$. (bottom) Corresponding electron distribution functions at the points indicated. The distribution functions were calculated using electrons in the z grid interval closest to the indicated points and within $0.072 \leq x \leq 0.074$.

(Figure 4, plots for $z = 3$ and 4), and then as the trailing edge of the pulse passes, the distribution function is decelerated back to the background Maxwellian (Figure 4, plots for $z = 5$ and 6). This implies that there must be regions of nonzero parallel electric field centered around $z = 2$ and 5 to accelerate and decelerate, respectively, the electron population. Exactly such a profile is shown in Figure 5a which illustrates the parallel electric field directly from the simulation at $t = 0.009$. We will return to a discussion of Figure 5b shortly.

3.2. Potential-Current Relation

[14] For consideration of the energy with respect to the electrons it is convenient to move to the frame of reference moving with the pulse (wave frame) where $\partial/\partial t = 0$ and so the system is to first order quasistatic. Considering again the pulse propagating toward $z = 0$ with speed $-V_A$, the velocity of an electron measured in the frame of reference of the pulse is given by

$$v_{ew} = v_e + V_A, \quad (10)$$

where v_e is the velocity of the electron in the plasma frame. The conservation of energy for the electron in the wave frame (in the absence of converging magnetic field) is then given by

$$\frac{1}{2}m_e v_{ew}^2 - e\phi_{\text{eff}} = U_e, \quad (11)$$

where ϕ_{eff} is the “effective” electrostatic potential (as the system is not exactly electrostatic since the curl of \mathbf{E} is not identically zero) and U_e is the electron’s total energy in the wave frame. For a population of cold electrons with number density n_e this can be expressed as

$$\frac{1}{2}\langle n_e m_e v_{ew}^2 \rangle - n_e e \phi_{\text{eff}} = W, \quad (12)$$

where the brackets are indicative of average and W is the total energy density. Using equation (10), this becomes

$$\frac{1}{2}n_e m_e (V_A^2 + 2\langle v_e \rangle V_A) - n_e e \phi_{\text{eff}} = W, \quad (13)$$

where $\langle v_e \rangle = -j_e/n_e e$ and the term v_e^2 was neglected since $v_e \ll V_A$. Far from the pulse, $j_e = 0$ and $\phi = 0$, which gives

$$W = \frac{1}{2}n_e m_e V_A^2. \quad (14)$$

Since pressure effects are negligible in a cold plasma, the energy density is conserved, and

$$\frac{1}{2}n_e m_e (V_A^2 + 2\langle v_e \rangle V_A) - n_e e \phi_{\text{eff}} = \frac{1}{2}n_e m_e V_A^2. \quad (15)$$

Substituting in for $\langle v_e \rangle$ in terms of j_e , this simplifies to

$$\phi_{\text{eff}} = -\frac{m_e j_e V_A}{n_e e^2}. \quad (16)$$

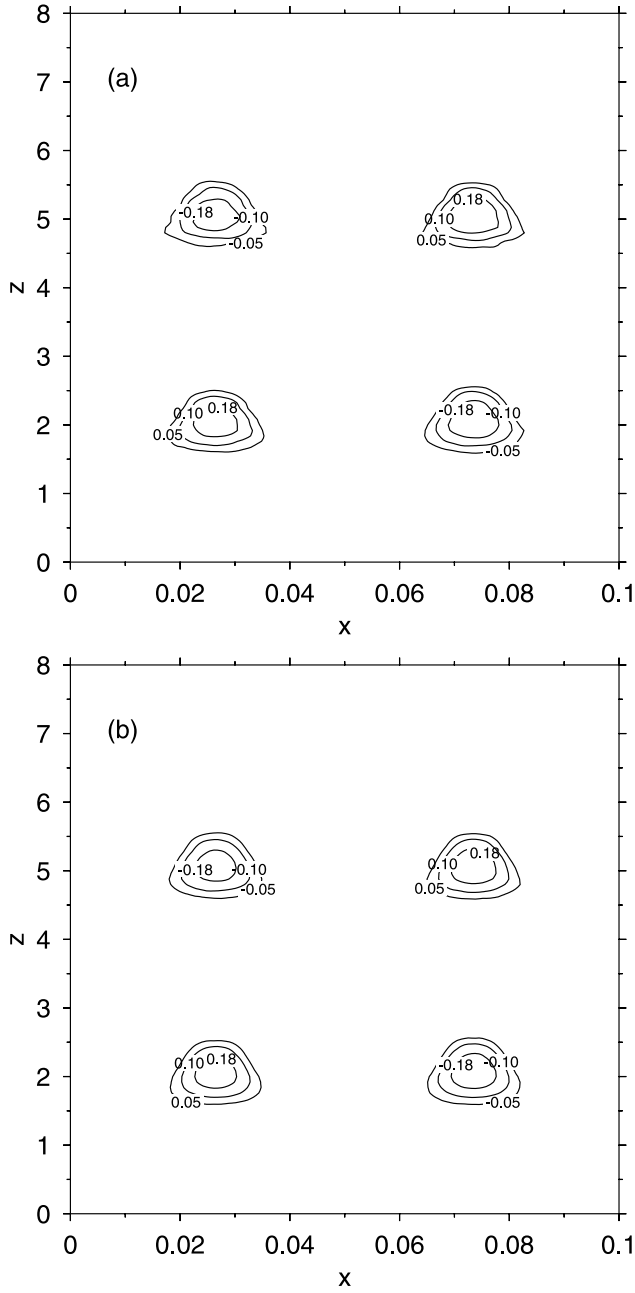


Figure 5. Contours of parallel electric field (a) calculated from the simulation and (b) calculated from the effective potential ϕ_{eff} at $t = 0.009$ for the $L_x = 100$ km case.

[15] Using the parallel current from Figure 3 and the corresponding profile for n_e from the simulation, the profile of the effective potential calculated using expression (16) is illustrated in Figure 6. Not surprisingly, it exhibits the same basic profile as the field-aligned current density. Now, calculating the parallel electric field from the potential using

$$E_z = -\frac{\partial\phi_{\text{eff}}}{\partial z}, \quad (17)$$

the results are displayed in Figure 5b. As is evident, this result agrees very well with the parallel electric field taken

directly from the simulation (plotted in Figure 5a), illustrating that the effective potential offers a good instantaneous picture of the parallel electric field. Since E_z is the same in the plasma and wave frames and we have made a linear approximation with regards to v_e , equation (16) reduces to the current-voltage relation for the linear fluid electron inertia term in the electron momentum equation $j_e = ie^2 n_e E_z / m_e \omega$ [i.e., see Rankin *et al.*, 1999]. This is accomplished with the assumption that $E_z = -ik_z \phi_{\text{eff}}$ and with the use of the shear Alfvén wave dispersion relation $\omega = -k_z V_A$. The exclusion of the nonlinear term in the momentum equation is justified since $\partial v_e / \partial t \gg (v_e \nabla_{\parallel}) v_e$ for a uniform equilibrium [Wright *et al.*, 2002].

4. Simulation in the Inertial Limit ($L_x = 25$ km)

[16] For the following simulation, $L_x = 25$ km was used, and the radial dimensions of the grid were reset to $0 \leq x \leq 0.04$ in nondimensional units. All other parameters remained the same. Figure 7 illustrates the parallel current at $t = 0.009$. As is evident, the contours are much more complicated than illustrated in Figure 3. Two main features are manifested. The first is a broadening of the pulse width at the leading edge and a narrowing at the trailing edge with the entire pulse length being greater than that exhibited for large L_x . The second feature is the appearance of small-amplitude waves propagating away from the pulse edges in the perpendicular direction. The small contour value of 50 (compared with the peak value of 1200) has been chosen to bring out these wave features, which are much more prominent in the contours of the parallel electric field to be discussed below. The smaller value of L_x implies that the parallel current should be larger, and this is evident in Figure 8, which is a slice along the center of the right-hand

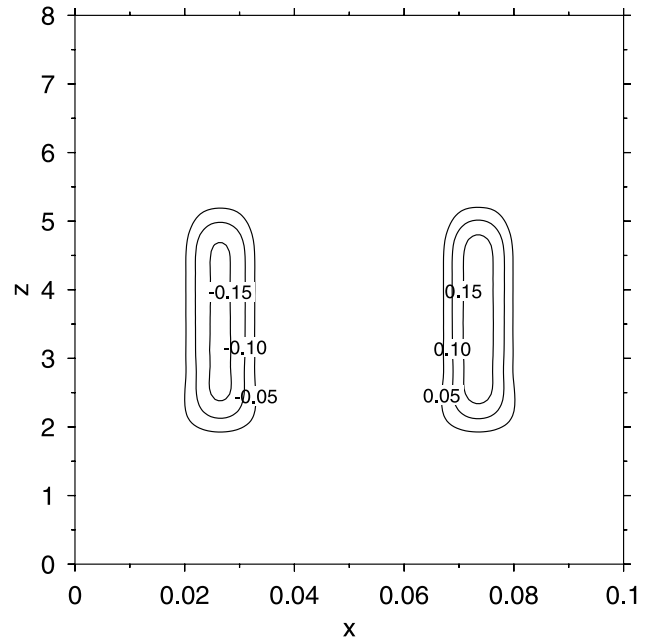


Figure 6. Contours of the effective potential ϕ_{eff} calculated from expression (16) using the parallel current illustrated in Figure 3b.

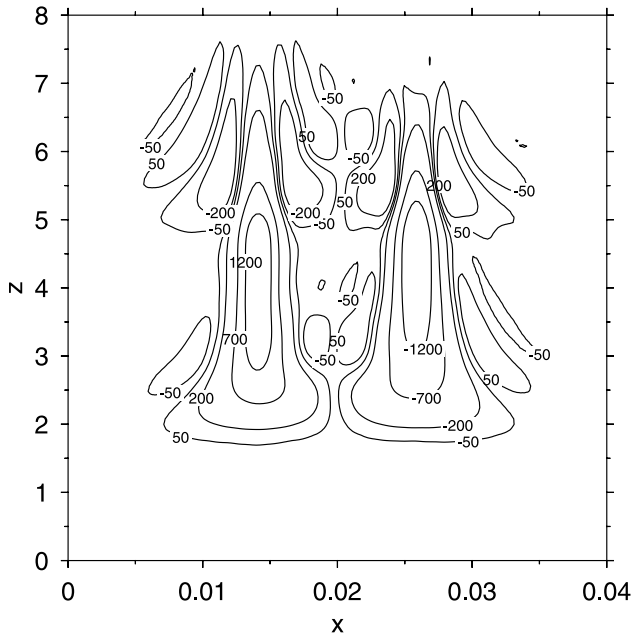


Figure 7. Contours of parallel electron current j_e at $t = 0.009$ for the $L_x = 25$ km simulation.

parallel current region at $x = 0.026$ along with the distribution functions at the points indicated. As is evident, the larger parallel current is carried by a larger displacement of the electron distribution function.

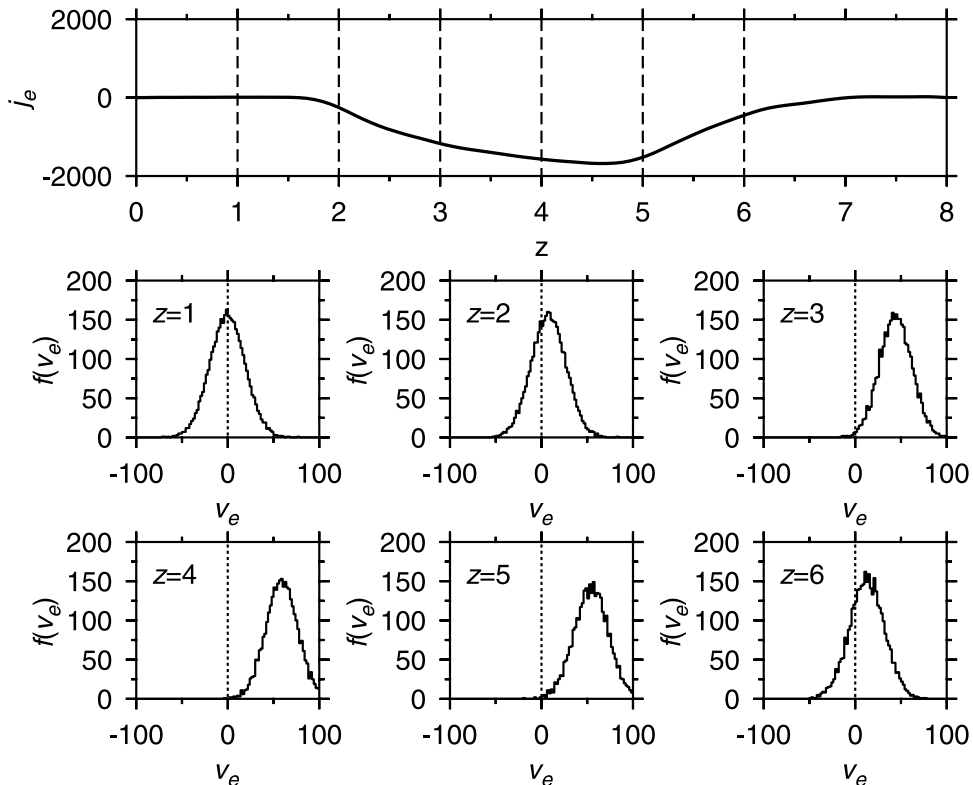


Figure 8. (top) Slice of parallel current density as a function of z at $x = 0.026$ and $t = 0.009$ for the $L_x = 25$ km case. (bottom) Corresponding electron distribution functions at the points indicated. The distribution functions were calculated using electrons in the z grid interval closest to the indicated points and within $0.025 \leq x \leq 0.027$.

[17] Figure 9 illustrates the parallel electric field at $t = 0.009$ from both the simulation (Figure 9a) and the electrostatic potential (Figure 9b) calculated in the same way as discussed in section 3.2. As with the current, the parallel electric field exhibits a broadening at the leading edges and a narrowing at the trailing edges along with the wave structure propagating away from the corners of the pulse in the perpendicular direction. Since we are in the limit $L_x \leq 10\lambda_e$, the inertial Alfvén wave dispersion relation applies, and these are inertial Alfvén waves with perpendicular wavelengths of the order of $10\lambda_e$ ($k_\perp \lambda_e \sim 1$). Such wave structures associated with Alfvén pulses are also evident in cold plasma theory (where they have been termed Alfvén resonance cones [Bellan, 1996; Stasiewicz *et al.*, 1997; Lysak and Song, 2001] and have also been noted in satellite observations [Stasiewicz *et al.*, 1997]). A better picture is illustrated in the plots at the bottom of Figure 9, which are slices of E_z as a function of x at $z = 2.96$ for both cases. The wavelength of the waves is ~ 50 km, which is of the expected order of $10\lambda_e$ (where $\lambda_e = 5.3$ km). In addition, comparison of Figures 5 and 9 illustrates the corresponding larger electric field needed to accelerate the electrons in the latter case.

[18] The fact that the quasi-static approximation still works in this regime is not surprising when one examines the electron and Alfvén timescales in the wave frame. For an electron the relevant timescale is simply the timescale needed to cross the region L_z , and as the electrons are moving with approximately the Alfvén speed in the wave

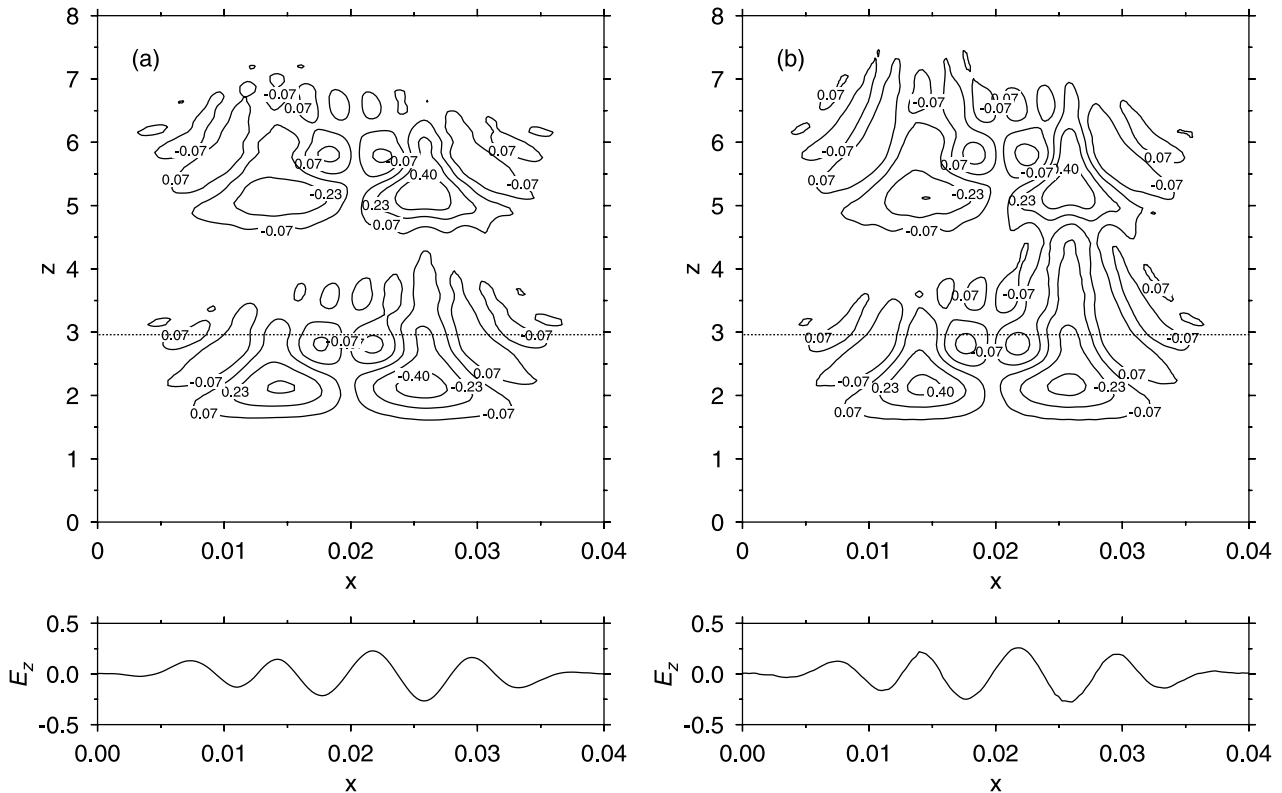


Figure 9. Contours of parallel electric field (a) calculated from the simulation and (b) calculated from the potential ϕ_{eff} at $t = 0.009$ for $L_x = 25$ km case. At the bottom are slices of E_z as a function of x at $z = 2.96$ (indicated by dotted line in the corresponding contour plot).

frame, the timescale $\tau_e = L_z/V_A = 0.002$ in nondimensional units. On the other hand, the Alfvén frequency in the wave frame is

$$\omega_{Aw} = \omega_{Ap} + k_z V_A = -\frac{k_z V_A}{\sqrt{1 + k_x^2 \lambda_e^2}} + k_z V_A, \quad (18)$$

where ω_{Ap} is the inertial Alfvén wave frequency in the plasma frame (note that k_z is less than zero, corresponding to propagation in the negative z direction with speed V_A). As is evident, in the MHD limit ($m_e \rightarrow 0$), $\omega_{Aw} = 0$ in this frame of reference, which is approximately the case in the large-scale limit. This implies that $\tau_{Aw} = 2\pi/|\omega_{Aw}| = \infty$, and so $\partial/\partial t$ is exactly 0. Therefore an observer moving with speed $-V_A$ would see no changes in the field values. In the inertial limit, though, ω_{Aw} has a nonzero value, and τ_{Aw} is finite, and an observer would see changes in this field on this timescale. Considering the dominant mode $k_x = 2\pi/L_x$, Figure 10 plots the ratio of the electron transit time to the Alfvén wave period as a function of L_x in units of λ_e . As L_x gets smaller, the Alfvén period approaches the electron transit time, and the quasi-static approximation breaks down. However, for the minimum parameters used here ($L_x \approx 5\lambda_e$), τ_{Aw} is ~ 3 times larger than τ_e , and so it is not surprising that the quasi-static approximation was still very good; that is, the wave fields do not change much during the electron transit. That the approximation breaks down for much smaller L_x was confirmed by a test run with $L_x \approx 2\lambda_e$, where the structure of parallel electric field determined from

the potential diverged fairly significantly from the simulation field.

[19] It should be noted that the true wave frame for the pulse is not moving with $-V_A$ but with the phase speed of the inertial Alfvén wave. For the large-scale limit this is a very good approximation which progressively gets worse as L_x gets smaller. It is not possible to transform to an inertial Alfvén wave frame, since the different k_x modes present will

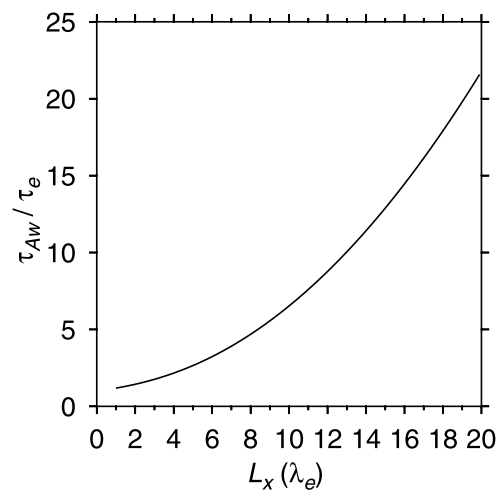


Figure 10. Ratio of Alfvén timescale (τ_{Aw}) to the electron transit timescale (τ_e) as a function of L_x where τ_{Aw} was calculated from expression (18) using $k_x = 2\pi/L_x$.

propagate in z at slightly different speeds, as evidenced by the evolved structure in Figure 7. However, the expression derived in the frame moving with the Alfvén speed reconstructed E_z very accurately for the perpendicular scales of interest, and the expression suggests that the error is small.

5. Energy

[20] The 2-D energy density (energy density per unit y) of the hybrid MHD-kinetic system in the plasma frame and for periodic boundary conditions is given in nondimensional units by (Damiano et al., submitted manuscript, 2004)

$$\frac{1}{2}\rho_0 u_y^2 + \frac{b_y^2}{2} + W_e, \quad (19)$$

where W_e is the kinetic energy density of the electrons (where the kinetic energy of an electron is $1/2m_e v_e^2$).

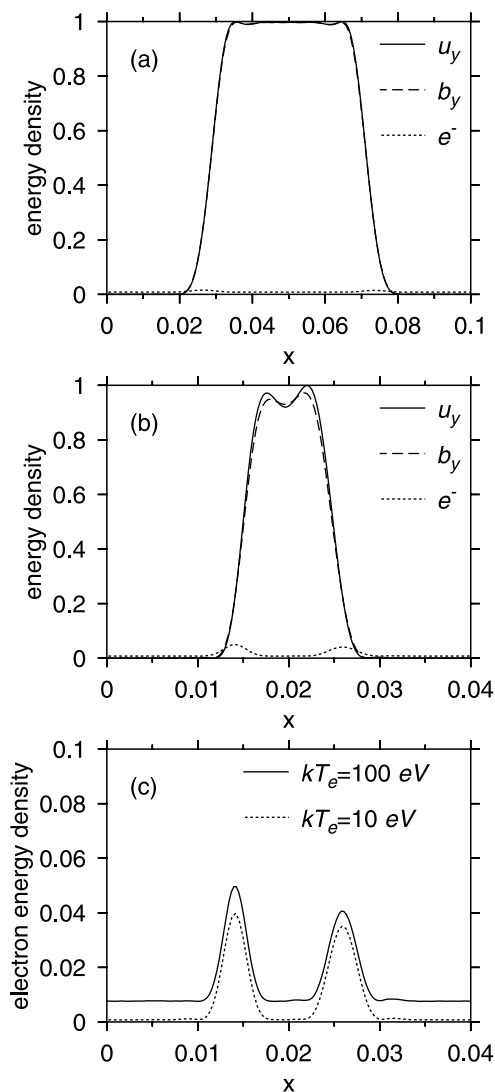


Figure 11. (a) Slices of the components of energy density at $z = 2.96$ for the $L_x = 100$ km case and (b) for the $L_x = 25$ km case. The densities in Figures 11a and 11b are normalized so that the maximum energy density in u_y is 1. (c) Electron energy density for the $L_x = 25$ km case and initial Maxwellian distribution function with $kT = 100$ eV (solid line) and $kT = 10$ eV (dotted line).

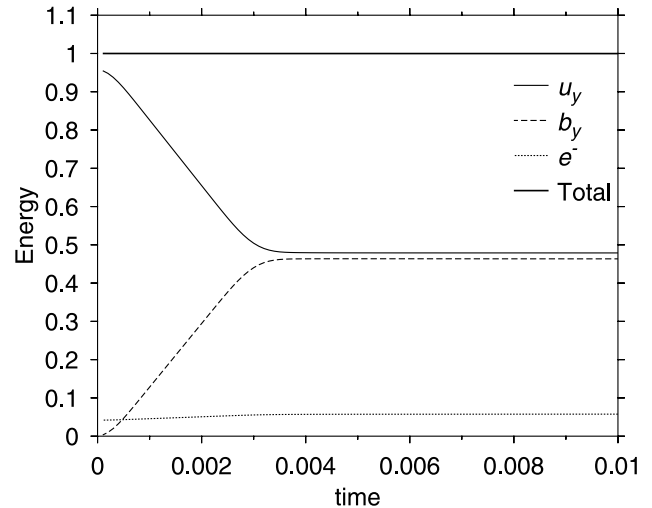


Figure 12. Energy as a function of time for the $L_x = 25$ km case.

Figure 11 illustrates a slice at $z = 2.96$ of the individual energy density terms as a function of x for $L_x = 100$ km (Figure 11a) and $L_x = 25$ km (Figure 11b). Both plots are for $t = 0.009$, and the slice at $z = 2.96$ was chosen because the current at this point is approximately average for the variation across the length of the pulse in z (see Figure 8) and therefore is more valid for comparison of average electron energy densities than the peak value. The densities are normalized so that the maximum energy density in u_y is 1. As is evident, there is relatively little energy residing in the electrons in the large perpendicular-scale limit, but for the inertial case they account for a more significant portion. Wright et al. [2003] show that the ratio of the electron energy density to the magnetic energy in the two-fluid picture can be expressed in terms of λ_e and L_x as

$$\frac{1/2nm_e\langle v_e \rangle^2}{b_y^2/2} \approx \frac{\lambda_e^2}{L_x^2}. \quad (20)$$

Using $\lambda_e = 5.3$ km and $L_x = 25$ km, the ratio is ~ 0.045 . This is consistent with the maximum values illustrated in Figure 11a. The two-fluid approximation works well here because of the large displacement of the entire distribution function. The shifting of the peak electrons with original velocity close to zero adds the largest contribution to the energy in the displaced picture, and consequently, the thermal energy residing in the width of the distribution (which is not incorporated in equation (20)) is of secondary importance. This is emphasized by the plot in Figure 11c of the electron energy density for the original simulation and a simulation with $kT = 10$ eV. In the $kT = 100$ eV case, there is a larger background energy density which would correspond to the thermal energy of the ambient distribution function, but it is still significantly less than the energy density associated with the shift in the distribution function. Also, the magnitude of the rise in energy density relative to the background is approximately the same in both cases, as expected.

[21] In Figure 12 the total energy is plotted as a function of time in the inertial case, illustrating that total energy is

nically conserved for the MHD-kinetic system as well. The gradual drop in the energy in u_y and the corresponding increase in the energy in b_y for $t \leq 0.003$ are due to the splitting of the initial perturbation which only had energy in u_y . In the large-scale limit, almost all the energy is split equally between the u_y and b_y modes, satisfying the Alfvén-Walén relation discussed in section 2, with a slight increase in the electron energy as the pulses separate and the currents emerge.

6. Summary and Discussion

[22] We have used the 2-D hybrid MHD-kinetic model of *Damiano et al.* [2003, also submitted manuscript, 2004] to consider the case of a rectangularly shaped Alfvén wave pulse propagating in a constant density plasma and magnetic field in both the large perpendicular-scale and inertial limits. In addition, we have derived a relation between the electrostatic potential and the parallel current density based on conservation of energy arguments in the frame of reference of the pulse, and a comparison was made between the parallel electric field determined from this potential and that produced directly from the model.

[23] In the limit of large perpendicular-scale length ($L_x = 100$ km) the pulse propagates with speed V_A and maintains its original geometry with slight modifications at the corners. The geometry of the pulse results in a clear separation of the perpendicular and parallel current regions around the edges of the pulse. Nonzero parallel electric field values appear at leading and trailing corners to accelerate the electrons to carry the parallel current along the edge and then decelerate them when the current edge region has passed. For the parameters considered here the entire distribution function is accelerated to carry the current. In this limit, as would be expected, the largest portion of the energy is by far concentrated in the u_y and b_y components with a small amount residing in the electrons.

[24] In the “inertial limit” ($L_x = 25$ km) the above simple picture becomes somewhat more complicated. The parallel current regions become more elongated in the parallel direction than in the large-scale limit and are broadened at the leading edge and narrowed at the trailing edge. In addition, small-amplitude inertial Alfvén waves with perpendicular wavelengths of the order of $10\lambda_e$ (Alfvén resonance cones) are seen to be propagating away from the leading and trailing corners of the pulse. These features are more clearly visible in the profile of the parallel electric field where, in addition to the inertial-scale structure, the oval profiles seen at the corners of the pulse in the large-scale limit broaden at their respective leading edges. Interestingly, though, the parallel electric field determined from the derived quasi-static potential-current relation still does a very good job of reproducing the simulation parallel electric field (as was the case in the large-scale limit). The smaller value of L_x also results in a stronger parallel current which is carried by a larger displacement of the electron distribution function. This large displacement means that the energy stored in the electrons becomes significant, and the almost exact equipartition of energy between the u_y and b_y components evident in the MHD limit breaks down. The proportion of energy residing in the electrons is in agreement with

the proportion predicted by the relation derived by *Wright et al.* [2003] using two-fluid theory. It should be noted that a Maxwellian background distribution function was chosen for simplicity, even though many examples in the magnetosphere are non-Maxwellian (i.e., Kappa distributions). However, the difference is probably not important since for these parameters the current is being carried by the shifting of the entire distribution function, and the shape is of secondary importance.

[25] Although this pulse simulation is not meant to be representative of ULF waves in the auroral acceleration region, the choice of parameters was designed to produce relatively realistic parallel current densities and spatial scales. In the $L_x = 100$ km case the maximum value of j_e is $\sim 0.6 \mu\text{A}/\text{m}^2$, and for $L_x = 25$ km the result was $j_e \sim 2 \mu\text{A}/\text{m}^2$. The energies of the electrons in the central shifted peaks of the distributions carrying this current were of the order of 50 and 500 eV for $L_x = 100$ and 25 km, and the corresponding peak parallel electric fields were ~ 0.6 and ~ 1 mV/m, respectively. These values for E_z are also of the order of magnitude that is expected for the acceleration of electrons by ULF waves. The electron energies are a little below the typical keV values associated with auroral arc formation. This is due to the fact that the initial b_y perturbation of 100 nT was divided equally between the two separating pulses. Thus the initial amplitude of each individual pulse is about half of typical values. If we were to double the b_y perturbation, that would double the parallel current density and quadruple the average electron energy, putting them comfortably in the keV range. Although it is beyond the scope of this model, such large drifts relative to the thermal velocity ($v_d \geq v_{th}$) minimize thermal effects and can give rise to a two-stream (Buneman) instability [*Buneman*, 1959; *Gary*, 1993]. However, we have chosen the somewhat small value of v_{th} not so much to reflect reality in the auroral acceleration region (where electron thermal energies can be of the order of a keV) but to emphasize the drift of the electron distribution function needed to carry the current. As well, in the case where the electron drift velocity becomes large enough to excite the Buneman instability, the net result is to thermalize the distribution function until it is warm enough that v_{th} is again in the range of stability [i.e., *Reitzel and Morales*, 1998], but this is a secondary effect which has no bearing on the initial displacement needed to carry the current. In terms of the general auroral electron acceleration problem the two-stream instability is not usually associated with downwelling beams in the auroral acceleration region (to which this work most applies) but most commonly with the case of cold upwelling beams accelerated by double layers close to the auroral ionosphere [*Newman et al.*, 2001]. These parameters are more favorable for the onset of the instability, and observations of intense electrostatic waves and nonlinear electron phase space hole structures are evidence of the presence of an instability [*Ergun et al.*, 2001].

[26] In summary, the work presents a clear and complete examination of what is happening in the hybrid picture during the propagation of a free Alfvén pulse in a uniform medium. It illustrates the usefulness of an effective potential to provide an accurate instantaneous picture of the parallel electric field in a wave frame for which the fields are approximately steady. The constant density assumption

neglects the effects of strong density gradients (and ionospheric reflection) evident in the Earth's acceleration region, and this will be more completely investigated in the future. However, since the use of the effective potential is dependent mostly on the timescales, it is possible that such a description is justified in the more complicated system, and it may be possible to construct a potential-current relation using a more complicated expression for electron energy. Also, although the geometry was idealized to clearly separate perpendicular and parallel current regions, such geometries can occur naturally in the shearing of magnetic field lines in plasma flow past a conducting body, such as in the wake of flow past Io [Wright and Southwood, 1987] or flow in the Earth's magnetosheath relative to the conducting ionosphere of the Earth [Wright, 1996].

[27] **Acknowledgments.** P.A.D. is funded by a PPARC grant. Simulations were conducted using the PPARC-funded St. Andrews Maths Cluster.

[28] Lou-Chuang Lee thanks Robert Lysak and Tim Yeoman for their assistance in evaluating this paper.

References

- Alfvén, H. (1942), On the existence of electromagnetic-hydrodynamic waves, *Ark. Mat. Astron. Fys.*, 29B(2), 1–7.
- Bellan, P. M. (1996), New model for ULF Pc5 pulsations: Alfvén cones, *Geophys. Res. Lett.*, 23, 1717.
- Birdsall, C. K., and A. B. Langdon (1991), *Plasma Physics via Computer Simulation*, Inst. of Phys. Publ., Bristol, U.K.
- Buneman, O. (1959), Instability, turbulence and conductivity in current-carrying plasma, *Phys. Rev.*, 115, 503.
- Chaston, C. C., C. W. Carlson, R. E. Ergun, and J. P. McFadden (2000), Alfvén waves, density cavities and electron acceleration observed from the FAST spacecraft, *Phys. Scr. T*, T84, 64.
- Chaston, C. C., J. W. Bonnell, L. M. Peticolas, C. W. Carlson, J. P. McFadden, and R. E. Ergun (2002), Driven Alfvén waves and electron acceleration: A FAST case study, *Geophys. Res. Lett.*, 29(11), 1535, doi:10.1029/2001GL013842.
- Chaston, C. C., J. W. Bonnell, C. W. Carlson, J. P. McFadden, R. E. Ergun, and R. J. Strangeway (2003), Properties of small-scale Alfvén waves and accelerated electrons from FAST, *J. Geophys. Res.*, 108(A4), 8003, doi:10.1029/2002JA009420.
- Cross, R. (1988), *An Introduction to Alfvén Waves*, Inst. of Phys. Publ., Bristol, U.K.
- Damiano, P. A., R. D. Sydora, and J. C. Samson (2003), Hybrid magneto-hydrodynamic-kinetic model of standing shear Alfvén waves, *J. Plasma Phys.*, 69, 277.
- Ergun, R. E., Y.-J. Su, L. Andersson, C. W. Carlson, J. P. McFadden, F. S. Mozer, D. L. Newman, M. V. Goldman, and R. J. Strangeway (2001), Direct observation of localized parallel electric fields in a space plasma, *Phys. Rev. Lett.*, 87, 045003, doi:10.1103/PhysRevLett.87.045003.
- Gary, S. P. (1993), *Theory of Space Plasma Microinstabilities*, Cambridge Univ. Press, New York.
- Goertz, C. K., and R. W. Boswell (1979), Magnetosphere-ionosphere coupling, *J. Geophys. Res.*, 84, 7239.
- Hui, C.-H., and C. E. Seyler (1992), Electron acceleration by Alfvén waves in the magnetosphere, *J. Geophys. Res.*, 97, 3953.
- Lotko, W., A. V. Streltsov, and C. W. Carlson (1998), Discrete auroral arc, electrostatic shock and suprathermal electrons powered by dispersive, anomalously resistive field line resonances, *Geophys. Res. Lett.*, 25, 4449.
- Lysak, R. L., and Y. Song (2001), A three-dimensional model of the propagation of Alfvén waves through the auroral ionosphere: First results, *Adv. Space Res.*, 28, 813.
- Lysak, R. L., and Y. Song (2002), Energetics of the ionospheric feedback interaction, *J. Geophys. Res.*, 107(A8), 1160, doi:10.1029/2001JA000308.
- Newman, D. L., M. V. Goldman, R. E. Ergun, and A. Mangeney (2001), Formation of double layers and electron holes in a current-driven space plasma, *Phys. Rev. Lett.*, 87, 255001, doi:10.1103/PhysRevLett.87.255001.
- Rankin, R., J. C. Samson, and V. T. Tikhonchuk (1999), Parallel electric fields in dispersive shear Alfvén waves in the dipolar magnetosphere, *Geophys. Res. Lett.*, 26, 3601.
- Reitzel, K. J., and G. J. Morales (1998), Dynamics of narrow electron streams in magnetized plasmas, *Phys. Plasmas*, 5, 3806.
- Rönmark, K. (2002), Auroral current-voltage relation, *J. Geophys. Res.*, 107(A12), 1430, doi:10.1029/2002JA009294.
- Samson, J. C., R. Rankin, and V. T. Tikhonchuk (2003), Optical signatures of auroral arcs produced by field line resonances: Comparison with satellite observations and modeling, *Ann. Geophys.*, 21, 1.
- Stasiewicz, K., G. Gustafsson, G. Marklund, P.-A. Lindqvist, J. Clemmons, and L. Zanetti (1997), Cavity resonators and Alfvén cones observed on Freja, *J. Geophys. Res.*, 102, 2565.
- Thompson, B. J., and R. L. Lysak (1996), Electron acceleration by inertial Alfvén waves, *J. Geophys. Res.*, 101, 5359.
- Walén, C. (1944), On the theory of sunspots, *Ark. Mat. Astron. Fys.*, 30A(15), 1–87.
- Wei, C. Q., J. C. Samson, R. Rankin, and P. Frycz (1994), Electron inertial effects on geomagnetic field line resonances, *J. Geophys. Res.*, 99, 11,265.
- Wright, A. N. (1996), Transfer of magnetosheath momentum and energy to the ionosphere along open field lines, *J. Geophys. Res.*, 101, 13,169.
- Wright, A. N., and A. W. Hood (2003), Field-aligned electron acceleration in Alfvén waves, *J. Geophys. Res.*, 108(A3), 1135, doi:10.1029/2002JA009551.
- Wright, A. N., and D. J. Southwood (1987), Stationary Alfvénic structures, *J. Geophys. Res.*, 92, 1167.
- Wright, A. N., W. Allan, M. R. Ruderman, and R. C. Elphic (2002), The dynamics of current carriers in standing Alfvén waves: Parallel electric fields in the auroral acceleration region, *J. Geophys. Res.*, 107(A7), 1120, doi:10.1029/2001JA900168.
- Wright, A. N., W. Allan, and P. A. Damiano (2003), Alfvén wave dissipation via electron energization, *Geophys. Res. Lett.*, 30(16), 1847, doi:10.1029/2003GL017605.
- Xu, B.-L., J. C. Samson, W. W. Liu, F. Creutzberg, and T. J. Hughes (1993), Observations of optical aurora modulated by resonant Alfvén waves, *J. Geophys. Res.*, 98, 11,531.

P. A. Damiano and A. N. Wright, Mathematical Institute, University of St. Andrews, St. Andrews KY16 9SS, UK. (pdamiano@mcs.st-and.ac.uk)